Whole life cycle of femtosecond ultraviolet filaments in water

Amélie Jarnac,[1] Gintaras Tamosauskas,[2] Donatas Majus,[2] Aurélien Houard,[1] André Mysyrowicz,[1]
Arnaud Couairon,[3,*] and Audrius Dubietis[2]

[1]*Laboratoire d'Optique Appliquée, ENSTA ParisTech, Ecole Polytechnique, CNRS, F-91762 Palaiseau, France*
[2]*Department of Quantum Electronics, Vilnius University, Sauletekio Avenue 9, Building 3, LT-10222 Vilnius, Lithuania*
[3]*Centre de Physique Theorique, CNRS, Ecole Polytechnique, F-91128 Palaiseau, France*

(Received 10 July 2013; published 7 March 2014)

We present measurements fully characterizing the whole life cycle of femtosecond pulses undergoing filamentation in water at 400 nm. The complete pulse dynamics is monitored by means of a four-dimensional mapping technique for the intensity distribution $I(x,y,z,t)$ during the nonlinear interaction. Measured events (focusing or defocusing cycles, pulse splitting and replenishment, supercontinuum generation, conical emission, nonlinear absorption peaks) are mutually connected.The filament evolution from laser energy deposition in water, which is of paramount importance for a wide range of technological and medical applications, is interpreted in light of simulation results.

DOI: 10.1103/PhysRevA.89.033809 PACS number(s): 42.65.Sf, 42.65.Re, 52.38.Dx, 52.50.Lp

I. INTRODUCTION

Laser energy deposition in liquids is the first stage of numerous applications, from bond breaking in chemical engineering and multiphoton induced chemistry to biomedical sciences [1,2]. In particular, safe noninvasive eye or brain laser surgery, lithotripsy, and laser-based cancer radiotherapy require high energies to be deposited in a narrow focal region by avoiding collateral damage [3–7]. Many investigations of laser energy deposition have been conducted with long (nanoscond) laser pulses or ultrashort (femtosecond) laser pulses with a low energy per pulse but tightly focused so as to reach high intensities in the focal region [8–11]. Laser energy deposition may be accompanied by several desired or unwanted physical phenomena such as propagation effects, ionization, single-shot or cumulative heating, generation of shock waves, and cavitation bubbles. Laser parameters, such as the central wavelength, pulse duration and energy, repetition rate, and focusing geometry, may allow for certain control of these phenomena, which is highly desirable for applications. Accurate control, however, requires a deep understanding of propagation dynamics to avoid undesirable effects, especially when the target is located in the bulk of living tissues or aqueous media.

With low numerical apertures, ultrashort laser pulses propagating in transparent media are now recognized to undergo strong pulse reshaping due to nonlinear effects [12,13]. A striking manifestation of this reshaping is supercontinuum generation, as reported with visible [14] and near-infrared (IR) femtosecond pulse propagation in water [15]. Spectral broadening is usually the signature of self-phase modulation due to the Kerr effect, which, in the space domain, leads to the formation of a filament, a narrow string of intense light that behaves as a diffraction-free beam over extended distances [16]. The first detailed observations of femtosecond filaments in water were performed with a laser pulse at wavelengths of 527 and 800 nm [17,18] and further investigated in [19] and [20]. Light-matter interaction during filamentation in water at 800 nm was accessed by time-resolved shadowgraphy [21,22]. In the visible and near-IR spectral range, laser energy deposition is initiated by multiphoton ionization and the subsequent propagation in the form of a filament involves nonlinear absorption, pulse splitting, supercontinuum generation, conical emission, and beam breakup, among other self-action effects revealed by numerical simulations [23,24] and experiments [25].

Ultraviolet (UV) light-matter interaction in transparent solids has indicated unexpected filamentation effects [26] including efficient deposition of laser energy to the medium. In the regime of two-photon absorption, this process is sustained by the quenching of pulse reshaping effects and the formation of a Bessel-like diffraction-free beam [27]. Although many promising applications are foreseen [1,2,4–7], the propagation of intense light pulses in living tissues and in water as a prototypical liquid, as far as medical and industrial applications are concerned, has not been investigated in the UV range, close to the minimum of water absorption.

In this paper, we report the first detailed experimental and numerical investigation of femtosecond UV laser pulses propagating in water. Our measurements, based on a time-resolved imaging technique [three-dimensional (3D) mapping] [28,29], not only allow us to characterize the pulse in three dimensions, whatever the complexity of the pulse structure, but also provide us the possibility of following the pulse during its nonlinear propagation, thus giving access to its full 4D (spatiotemporal) evolution. This shows the intimate links between complex propagation effects: pulse splitting into subpulses, conical emission, supercontinuum generation, and transmittance and laser energy deposition for different focusing geometries and submicrojoule pulse energies, backed up by theoretical interpretation guided by numerical simulations.

II. SETUP FOR LASER PULSE INTENSITY MEASUREMENTS IN FOUR DIMENSIONS

The experimental setup is shown in Fig. 1. We used an amplified Ti:sapphire laser system (Spitfire PRO; Newport-Spectra Physics), which provides few-milijoule pulses at

*couairon@cpht.polytechnique.fr

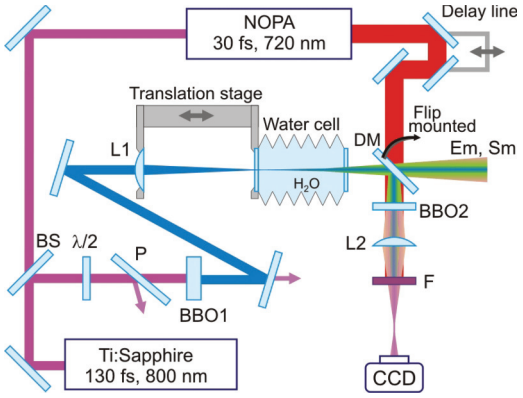

FIG. 1. (Color online) Experimental setup. BS, beam splittter; P, polarizer; L1, focusing lens (focal length: 50, 200, or 300 mm). BBO1 and BBO2 are β-barium borate crystals used for second-harmonic generation producing an input pulse at 400 nm and for difference frequency generation between the filament and the 30-fs reference pulse from the noncollinear optical parametric amplifier (NOPA), respectively. The length of the water-filled cell is variable between 4 and 40 mm. DM, dichroic mirror; Em, energy meter; Sm, spectrometer; F, filter.

800 nm with a duration of 130 fs. The laser output was divided into two parts by means of a beam splitter. The first part of the split beam was used for filament generation. A suitably attenuated laser pulse (by means of a half-wave plate $\lambda/2$ and a polarizer P) was frequency doubled via second-harmonic generation in a 1-mm-thick β-barium borate crystal (BBO1), which produced an input UV 400-nm, 10-fs pulse with an FWHM beam diameter of 1 mm. Thereafter the input beam was focused on the front window of a water-filled cuvette of tunable length. The front window of the cuvette and the focusing lens L1 were fixed together on the translation stage, thus allowing us to change the length of the cuvette, at the same time, preserving a fixed focal position, while the output window remained unmovable. The energy of the input pulse was varied from 70 nJ to 1 μJ, which corresponded to an input power range from 0.6 to 9 P_{cr} for which no beam breakup into several hot spots or multiple filamentation was observed. The spatiotemporal profile of the pulse at the cuvette output was recorded by means of the 3D mapping technique [28,29]. A short, 30-fs, reference pulse with a central wavelength of 720 nm was generated in a noncollinear optical parametric amplifier (NOPA; Topas-White; Light Conversion Ltd.), which was pumped by the rest of the laser energy. The filament was superimposed with the reference beam by the use of a dichroic mirror, which was mounted on a flipping stage. Specifically, the 3D images of the filament were retrieved by sampling the filament with a short reference pulse by means of difference-frequency generation in a 20-μm-thick β-barium borate crystal (BBO2) cut for type I phase matching. Filter F (RG850) was used to transmit only the difference-frequency signal with a center wavelength of 900 nm, and lens L2 was positioned so as to form a backimage of the difference-frequency signal on the CCD camera (JAI A-1); see [30] for details. By changing the time delay of the reference pulse in a 10-fs step, a sequence of spatially resolved cross-correlation images was acquired, which afterwards were merged together to reproduce the spatiotemporal intensity distribution of the filament. Changing the length of the cuvette from 4.5 to 40 mm, i.e., the length of nonlinear propagation z, allowed us to follow the evolution of the pulse along the propagation direction and reconstruct its intensity distribution $I(x,y,t,z)$ in four dimensions. We characterized the formation of filaments and pulse-splitting events for three focusing geometries (focal lengths of L1: 50, 200, and 300 mm), which corresponded to numerical apertures of 0.017, 0.0043, and 0.0028, respectively. In the same setup, by flipping the dichroic mirror, transmission, supercontinuum emission, and conical emission were recorded as functions of the length of the cuvette using a calibrated photodiode with a wavelength sensitivity correcting filter, which served as an energy meter, fiber spectrometer (Sm; QE65000; Ocean Optics), and digital photocamera, respectively. The combined measurements uncover the whole life cycle of ultrashort pulses undergoing filamentation in water at 400 nm.

III. PULSE RESHAPING DURING FILAMENTATION

The first panel in Fig. 2 shows the 4D reconstruction of the intensity distribution of a 100-nJ pulse propagating in water under loose focusing conditions (L1: 300 mm). The initially ovoid intensity distribution undergoes pulse splitting after propagation over 23–24 mm in water. During the splitting event, a ring is formed in the center of the pulse. The split pulses move away from the center, while the ring rebuilds the axial pulse at $t = 0$ [Figs. 2(e)–2(g)]. Thereafter the whole spatiotemporal formation increases in dimension as a result of diffraction.

Successive multiple splitting events separated by refocusing stages were observed by increasing the input pulse energy. For instance, a 400-nJ pulse under the same focusing conditions undergoes pulse splitting at $z \sim 8$ mm, $z \sim 11$ mm, and $z \sim 16$ mm. The splitting events are best monitored by the presence of a ring-like structure in the central part of the pulse. The split pulses are clearly visible when the leading and trailing pulses separate before the light contained in the ring refocuses on the axis. Figures 3(a), 3(c), 3(e), and 3(h) clearly show the ring structure, while split pulses are clearly visible in Figs. 3(e), 3(g), and 3(h). Refocusing processes are also clearly monitored in Figs. 3(b), 3(d), and 3(f) between splitting events.

Three successive pulse-splitting events were also observed for a pulse with an input energy of 450 nJ by using a tighter focusing geometry (L1: 200 mm), as shown in Figs. 4(a), 4(d), and 4(g). This temporal dynamics is associated with changes in supercontinuum emission and in conical emission. Splitting events are associated with signatures in the axial spectra, presented in Figs. 5(A)–5(C). After the first splitting event is detected for a length of 8 mm, a strongly red-shifted supercontinuum is generated [Fig. 5(A)], in contrast with all previous measurements of supercontinuum generation induced by a pulse in the IR or the visible region [14,15,17]. After the second splitting event (length of 11 mm), the supercontinuum spectrum becomes modulated and the modulation is particularly pronounced on the red side [Fig. 5(B)]. The periodic modulation occurs as a result of interference between the primary and the secondary split pulses. After the third

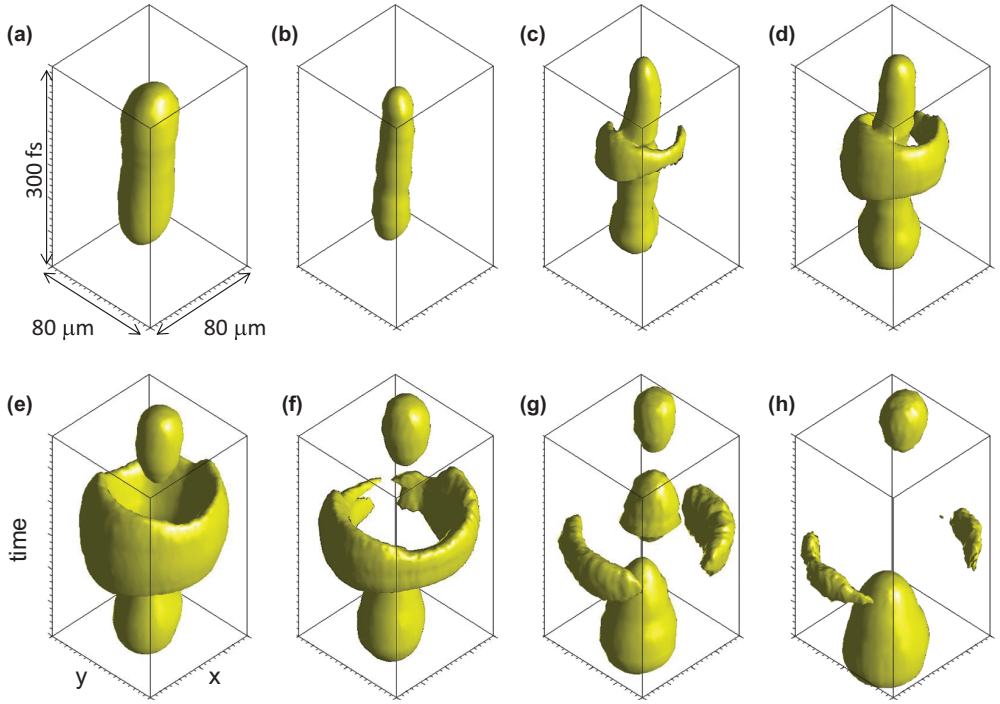

FIG. 2. (Color online) Measured intensity distributions for a 400-nm, 100-fs laser pulse undergoing filamentation and pulse-splitting events in water. $E_{in} = 100$ nJ; L1, 300 mm. Plots show surfaces at intensity levels 20% of the peak intensity for propagation distances of (a) 19 mm, (b) 21 mm, (c) 23 mm, (d) 24 mm, (e) 26 mm, (f) 28 mm, (g) 30 mm, and (h) 32 mm in water. Box size: 80 μm × 80 μm × 300 fs. Propagation direction: from top to bottom.

splitting event (length of 17 mm), the modulation in the supercontinuum spectrum has beatings contributed by the occurrence of a tertiary split pulse [Fig. 5(C)]. Figure 5(D) shows the transitions in the measured supercontinuum for a 450-nJ pulse undergoing filamentation in water. Discontinuities are marked by red-shifted spectral broadening and the appearance of modulations and beatings, which coincide with splitting events.

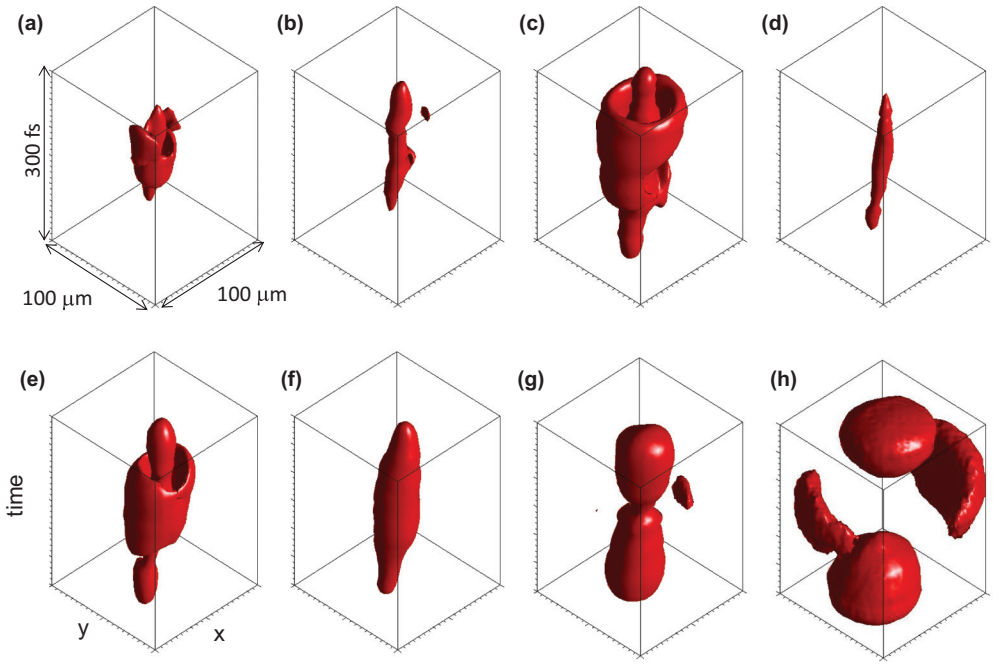

FIG. 3. (Color online) Measured intensity distributions for a 400-nm, 100-fs, 400-nJ laser pulse undergoing filamentation and pulse-splitting events in water. Focusing geometry L1: 300 mm. Plots show surfaces at intensity levels 20% of the peak intensity for propagation distances of (a) 9 mm, (b) 11 mm, (c) 14 mm, (d) 15 mm, (e) 17 mm, (f) 21 mm, (g) 31 mm, and (h) 33 mm. Box size: 100 μm × 100 μm × 300 fs. Propagation direction: from top to bottom.

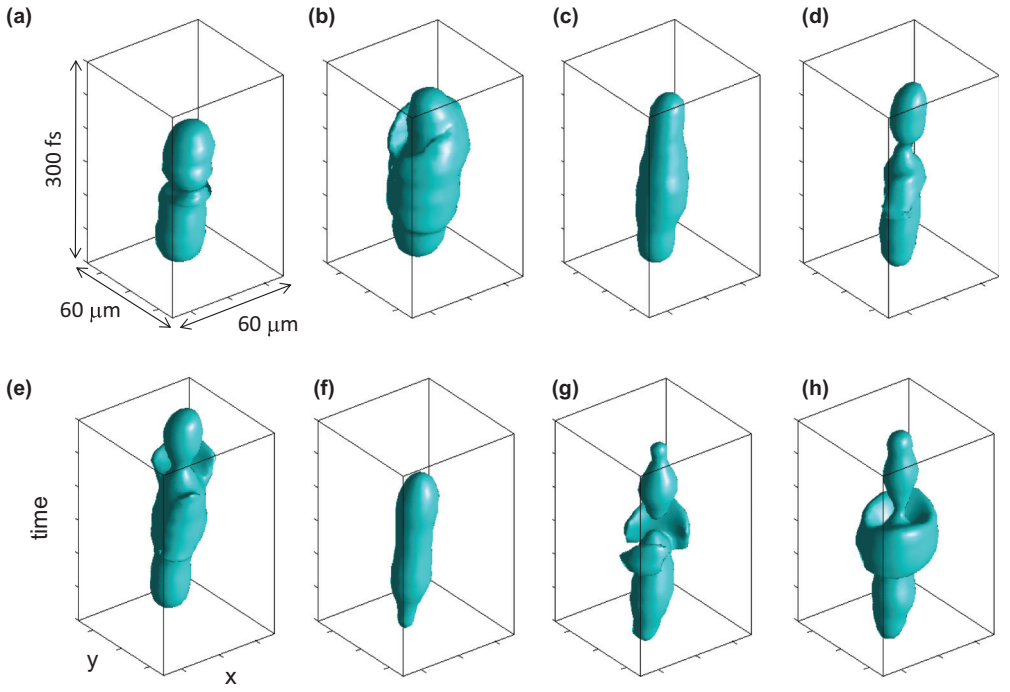

FIG. 4. (Color online) Measured intensity distributions for a 400-nm, 100-fs laser pulse undergoing filamentation and pulse-splitting events in water. $E_{\text{in}} = 450$ nJ; L1, 200 mm; and propagation distances of (a) 8 mm, (b) 9 mm, (c) 10 mm, (d) 12 mm, (e) 13 mm, (f) 16 mm, (g) 17 mm, and (h) 18 mm. Box size: 60 μm × 60 μm × 300 fs. Propagation direction: from top to bottom.

Very similar, almost-identical spectral features were recorded for pulse energies exceeding the threshold for multiple splitting and for all focusing geometries. They were observed in the far field as well. Figures 5(a)–5(c) show conical emission for a 450-nJ initial pulse loosely focused in water (L1: 200 mm). Figure 5(a) shows a smooth conical emission pattern after the first splitting event. Previous works reported a self-cleaning effect during filamentation in air [31,32]. Observation of a similar phenomenon in water not only indicates its universality, independently of the medium, but also reveals a nice signature of the elusive temporal dynamics within the filament: conical emission becomes regularly modulated after two splitting events [Fig. 5(b)] and exhibits irregularly spaced rings after three splitting events [Fig. 5(c)]. The best visibility of these features was obtained for the smallest numerical aperture of 1/300 and an input energy of 400 nJ.

The 4D mapping of the pulse intensity $I(x,y,z,t)$ enabled us to reconstruct the fluence profile $F(r,\theta,z) \equiv \int I(r\cos\theta, r\sin\theta, z, t)\,dt$. From this quantity, we calculated the beam diameter $D(z) \equiv \langle 2R_\theta(z)\rangle$, defined as the θ-averaged FWHM of the fluence distribution, where $R_\theta(z)$ is defined as $F(R_\theta(z),\theta,z) = 0.5F_{\max}(z)$, with $F_{\max}(z) \equiv \max_{r,\theta}[F(r,\theta,z)]$. Figure 6 shows the evolution of the beam diameter, output spectrum, and transmitted energy as functions of the propagation distance in water (cuvette length) in the case of loose focusing. These diagnostics exhibit a striking coincidence between beam pinching [transition between focusing and defocusing cycles; see Fig. 6(a)], the appearance of significant spectral broadening or spectral modulations [Fig. 6(b)] following the splitting events monitored by the 3D mapping technique, and the sudden decrease in the transmittance [lower (blue)] curve marked by the dips in the absorption rate [upper (red) curve] in Fig. 6(c). These diagnostics all constitute signatures of pulse-splitting events.

IV. NUMERICAL SIMULATIONS

A. Model

The model used for numerical simulations consists in a 3D unidirectional propagation equation with cylindrical symmetry for the nonlinear envelope $E(t,r,z)$ coupled with an evolution equation for the electron density $\rho(t,r,z)$ generated by the high-intensity pulse. The variables t, r, and z denote the pulse local time, the radial coordinate, and the propagation distance, respectively. Water is a dispersive medium characterized by a frequency-dependent refractive index $n(\omega)$ and a dispersion relation $k(\omega) \equiv n(\omega)\omega/c$. We use conventional notations for the refractive index $n_0 \equiv n(\omega_0)$, wave number $k_0 = k(\omega_0)$, and inverse group velocity $k_0' \equiv (\partial k/\partial\omega)_{\omega_0}$ at the central laser frequency ω_0. We define the dispersion function $\mathcal{K}(\omega) \equiv k(\omega) - k_0 - k_0'(\omega - \omega_0)$ and the nonlinear dispersion function $\mathcal{Q}(\omega) = \omega^2/k(\omega)c^2$. One of the most convenient ways to implement dispersion functions in the pulse propagation equation is in the frequency domain. We consider the frequency components $\mathcal{E}(\omega,r,z) \equiv \mathcal{F}[E(t,r,z)]$ for the electric-field envelope, where $\mathcal{F}$ denotes Fourier transform from the temporal to the spectral domain. The propagation equation takes the canonical form [33]:

$$\frac{\partial\mathcal{E}}{\partial z} = i\mathcal{K}(\omega)\mathcal{E} + \frac{i}{2k(\omega)}\nabla_\perp\mathcal{E} + i\mathcal{Q}(\omega)\frac{\mathcal{P}}{2\epsilon_0} - \frac{\mathcal{J}}{n(\omega)2\epsilon_0 c}, \tag{1}$$

where the nonlinear polarization $\mathcal{P}(\omega,r,z) \equiv \mathcal{F}[P(t,r,z)]$, with $P \equiv 2\epsilon_0 n_0 n_2 IE$, describes the response of a Kerr

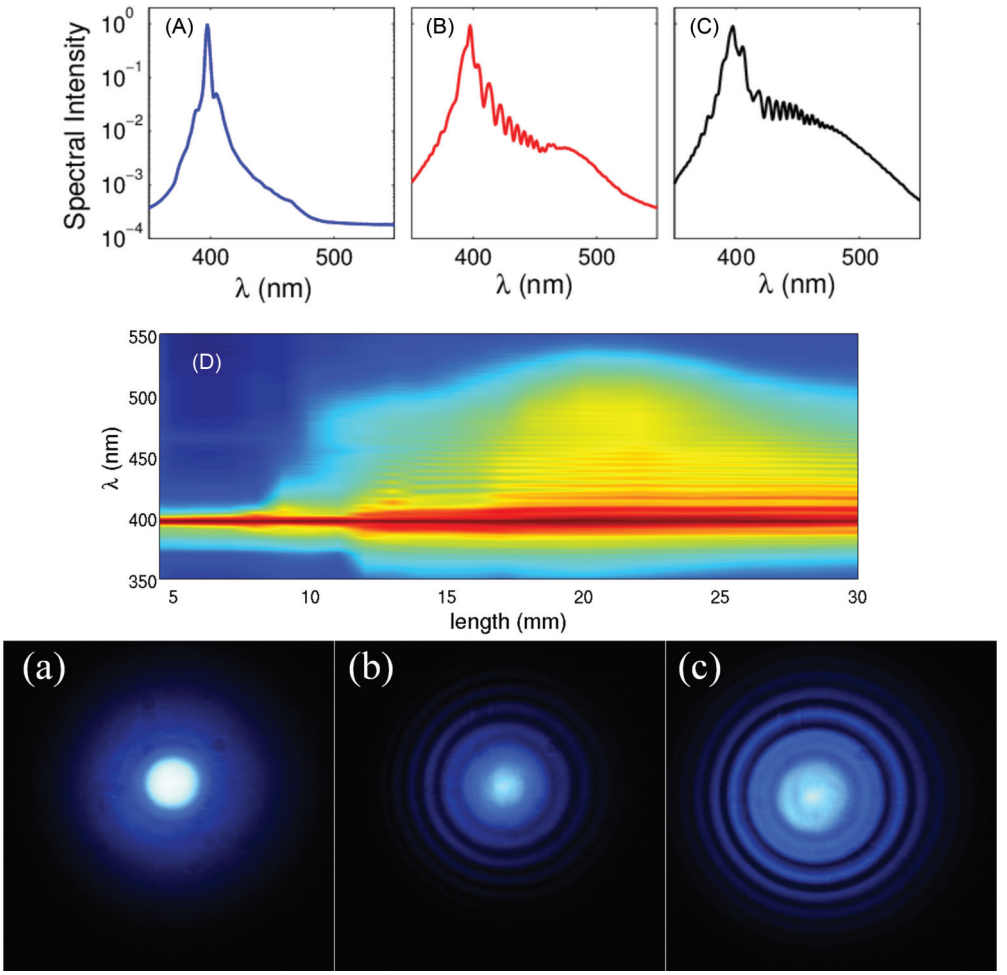

FIG. 5. (Color online) Supercontinuum spectra (A–C) as a function of propagation distance (D) and conical emission patterns (a–c) for a 450-nJ initial pulse focused in water (L1: 200 mm), showing modulations that appear after splitting events. Propagation distances in water are (A) $z = 9$ mm, (B) $z = 13$ mm, (C) $z = 17$ mm, (a) 12 mm, (b) 14 mm, and (c) 16 mm.

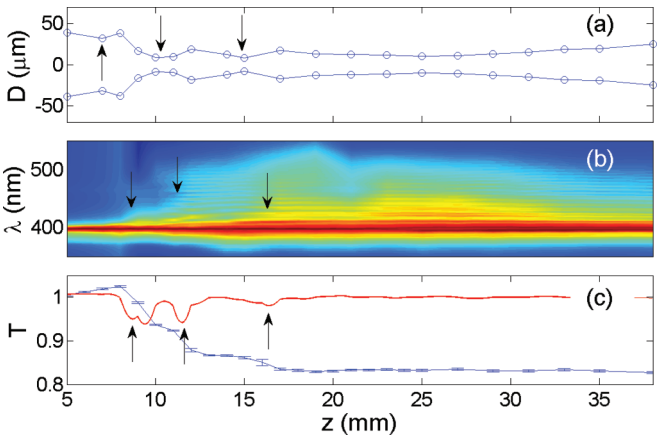

FIG. 6. (Color online) Typical signatures of pulse splitting for filaments generated in water for loose focusing conditions (L1: 300 mm), a pulse of 400 nm and 100 fs, and $E_{\text{in}} = 400$ nJ. (a) Beam diameter, (b) supercontinuum, and (c) transmittance as functions of the propagation distance. Arrows indicate a pinching of the beam diameter, significant spectral broadening or the appearance of modulations in the spectrum, and an increase in nonlinear losses that coincide with each pulse-splitting event ($z = 8$, 11, and 16 mm).

medium with nonlinear index coefficient n_2 for a pulse of intensity $I \equiv (1/2)\epsilon_0 c n_0 |E|^2$. The current $\mathcal{J}(\omega,r,z) \equiv \mathcal{F}[J(t,r,z)]$, where $J \equiv J_{\text{MPA}} + J_{\text{PL}}$ comprises two contributions due to multiphoton absorption (MPA) and plasma-induced effects (PLs). The current describing MPA reads $J_{\text{MPA}} = \epsilon_0 c n_0 \beta_K I^{K-1} E$, with coefficient β_K and number of photons K. PLs, i.e., plasma absorption and plasma defocusing, are included in a single expression for the current $\mathcal{J}_{\text{PL}}(\omega,r,z) = \epsilon_0 c \sigma(\omega) \mathcal{F}[\rho E]$ with complex-valued coefficient $\sigma(\omega)$, the real part of which, σ_r, corresponds to the cross section for inverse Bremsstrahlung in the Drude model,

$$\sigma(\omega) \equiv \frac{\omega_0^2 \tau_c}{c\rho_c} \frac{1}{1 - i\omega\tau_c}, \tag{2}$$

where τ_c denotes the collision time in water, and ρ_c the critical plasma density beyond which the medium is no longer transparent. The quantity $\omega_0^2/c\rho_c$ is a constant ($q_e^2/c\epsilon_0 m \sim 0.1$ cm^2/s) which does not depend on the laser central frequency. The evolution of the electron plasma density is modeled by a rate equation modeling multiphoton and avalanche ionization, as well as recombination with

TABLE I. Parameter values used in the model, Eqs (1) and (3).

Refraction index	n_0	1.34	[34]
Dispersion relation	$k(\omega)$	—	[34]
Kerr index coefficient	n_2 (cm^2/W)	4.1×10^{-16}	[35]
Number of photons	K	3	$\left\langle \frac{U_i}{\hbar\omega_0} + 1 \right\rangle$
MPA coefficient	β_3 (cm^3/W^2)	5.4×10^{-24}	[36]
Gap	U_i (eV)	6.5	[37]
Collision time	τ_c (fs)	1	[37]
Recombination	η_r (cm^3/s)	2×10^{-9}	[8]
Neutral density	$\rho_{\rm nt}$ (cm^{-3})	6.7×10^{22}	[37]
Critical plasma density	ρ_c (cm^{-3})	7.0×10^{21}	

rate η_r:

$$\frac{\partial \rho}{\partial t} = \left(\frac{\beta_K}{K\hbar\omega_0} I^K + \frac{\sigma_r(\omega_0)\rho I}{U_i} \right)\left(1 - \frac{\rho}{\rho_{nt}}\right) - \eta_r \rho^2. \quad (3)$$

We, finally, provide Table I, which lists the model parameters used for water and a pulse central wavelength of 400 nm, together with references from which values were obtained. The dispersion relation of water is Eq. (3) from Ref. [34]. We note that recent measurements of the Kerr index coefficient in water provided values different from those in Ref. [35], namely, $n_2 = 2.7 \times 10^{-16}$ cm^2/W at 532 nm in Ref. [38] and $n_2 = 1.7 \times 10^{-16}$ cm^2/W at 407 nm in Ref. [39]. The best comparison of numerical results with the experiments was obtained for $n_2 = 4.1 \times 10^{-16}$ cm^2/W [35].

We, finally, justify the use of multiphoton ionization rates rather than the Keldysh formulation, which is considered to be more accurate. Figure 7 represents the ionization rates as a function of the intensity. The complete Keldysh formulation, represented as the thick black curve, has two distinct asymptotes: the multiphoton limit at low intensity and the tunnel limit at high intensity. The multiphoton limit takes a simple form, $W(I) = \sigma_3 I^3$, which remains undistinguishable from Keldysh's ionization rates for intensities up to 7×10^{13} W/cm^2. This intensity level is not reached in any of our simulations, therefore, the use of multiphoton ionization rates in our model is fully equivalent to the use of Keldysh's ionization rates.

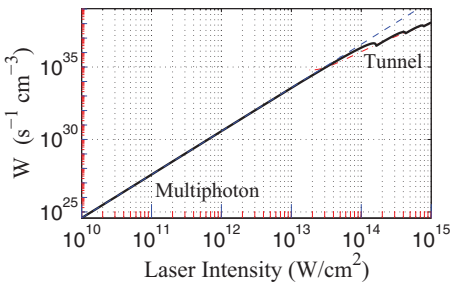

FIG. 7. (Color online) Ionization rates as a function of the laser intensity in water, at the central wavelength of 400 nm. Thick curve: complete Keldysh's formulation. Upper dashed (blue) curve: multiphoton ionization rate $W(I) = \sigma_3 I^3$ asymptotic to the Keldysh ionization rates. Lower dashed (red) curve: tunnel ionization rate.

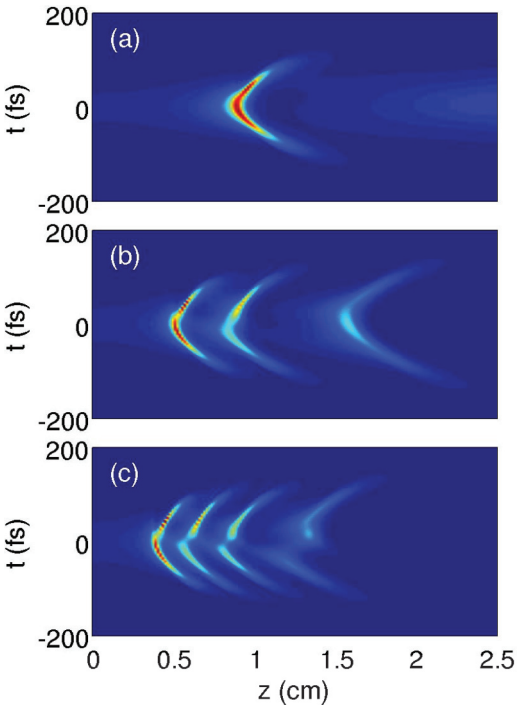

FIG. 8. (Color online) Temporal profiles for the axial intensity distribution $I(t,r=0,z)$ from numerical simulation of the propagation in water of a UV (400-nm) initial pulse with an energy of (a) 200 nJ, (b) 400 nJ, and (c) 600 nJ. The pulse duration is 90 fs. Other parameters correspond to the experiments under loose focusing conditions (L1: 300 mm).

B. Interpretation of numerical simulations

Figure 8 shows the pulse-splitting dynamics for a UV pulse propagating in water. The simulated axial intensity profile $I(t,r=0,z)$ is shown as a function of the propagation distance z, under the conditions of our experiments in loose focusing conditions (L1: 300 mm). An increasing number of pulse-splitting events is obtained for increasing input energies. The number of pulse-splitting events is in good agreement with the measurements. A striking feature of the splitting dynamics is the quasisymmetric pattern obtained for each splitting event. As in the measurements, splitting events always lead to two split pulses. The leading intensity peak is a superluminal split pulse (it propagates toward negative times) and the trailing peak is a subluminal split pulse (it propagates toward positive times). This quasisymmetry suggests that the main effect responsible for the splitting event is MPA. If plasma defocusing played a stronger role in this dynamics, it would lead to an asymmetry in the splitting process: the leading split pulse would first appear and propagate superluminally. The trailing pulse would appear later, only once the leading pulse decays due to MPA, eventually followed by a refocusing process of a central pulse undergoing the same dynamics. This would result in successive splitting events leading to a single pulse rather than two coexisting split pulses at a given distance. The main role of MPA is further confirmed by the fact that spectra were essentially red-shifted after splitting events, whereas plasma defocusing would be responsible for the generation of new frequencies on the blue side of the laser spectrum.

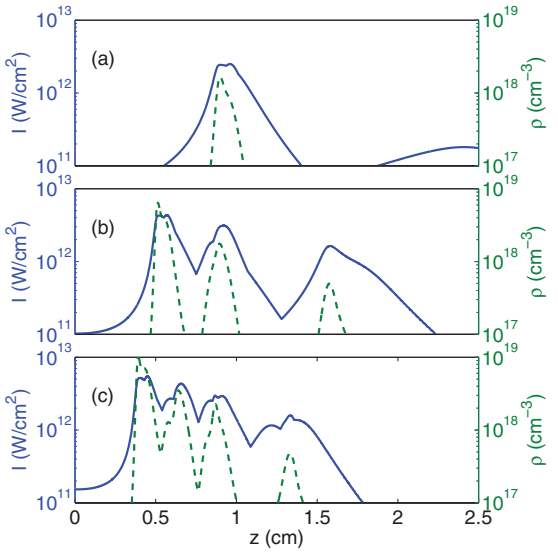

FIG. 9. (Color online) Maximum intensity (solid curves) and electron density (dashed curves) as functions of the propagation distance for simulations with the same parameters as in Fig. 8. Pulse energy: (a) 200 nJ, (b) 400 nJ, and (c) 600 nJ.

Figure 9 shows the peak intensity and electron densities obtained in the simulations corresponding to Fig. 8. The maximum intensity does not exceed 6×10^{12} W/cm^2, justifying that multiphoton ionization rates coincide with the complete Keldysh formulation. The maximum electron density always remains below 10^{19} cm^{-3} and exceeds 10^{18} cm^{-3} only in very localized regions. Although the lowest local refractive index change due to this plasma density is approximately -5×10^{-4}, a value nearly opposite to the refractive index change induced by the Kerr effect at the higest intensity, the defocusing effect of the plasma is delayed with respect to the peak intensity and therefore can only affect the trailing part of the pulse. In contrast, MPA is an instantaneous effect acting on the intense part of the pulse and leads to quasisymmetric splitting events when it is the key player.

In order to illustrate the difference in the pulse dynamics induced by plasma defocusing versus by MPA, we show simulation results in Fig. 10 which were obtained for the same parameters but with the value of the nonlinear index coefficient corresponding to the latest measurement [39] and the pulse energies increased to obtain roughly the same number of splitting events as in the measurements. The first important difference is that the energy range necessary to reproduce these splitting events is significantly higher than that of the measurements. The second difference concerns the asymmetry in the splitting events. Except for the lowest energy of 1 μJ, higher energy pulses do not exhibit two split pulses at a given propagation distance, but a single leading or trailing pulse with a possible pedestal. Such extreme situations were not found in our measurements. In these asymmetric cases, we interpret plasma defocusing as playing a more important role in the splitting events, as also suggested by the longer plasma channels compared to Fig. 9.

In summary, the number of pulse-splitting events, the shape of the split pulses, and their quasisymmetry are best reproduced by our numerical simulations performed with the nonlinear index coefficient $n_2 = 4.1 \times 10^{-16}$ cm^2/W [35]. The good matching of the positions of simulated and measured symmetric splitting events indicates that the plasma does not play an important role in the splitting dynamics, in keeping with the fact that plasma-induced self-phase modulation would have led to a blue-shifted supercontinuum, whereas measurements have shown a marked red shift.

V. DISCUSSION

From our observations and guided by the simulation results, we interpret the respective roles of MPA and plasma defocusing in the pulse-splitting dynamics. Figure 8(b) shows the

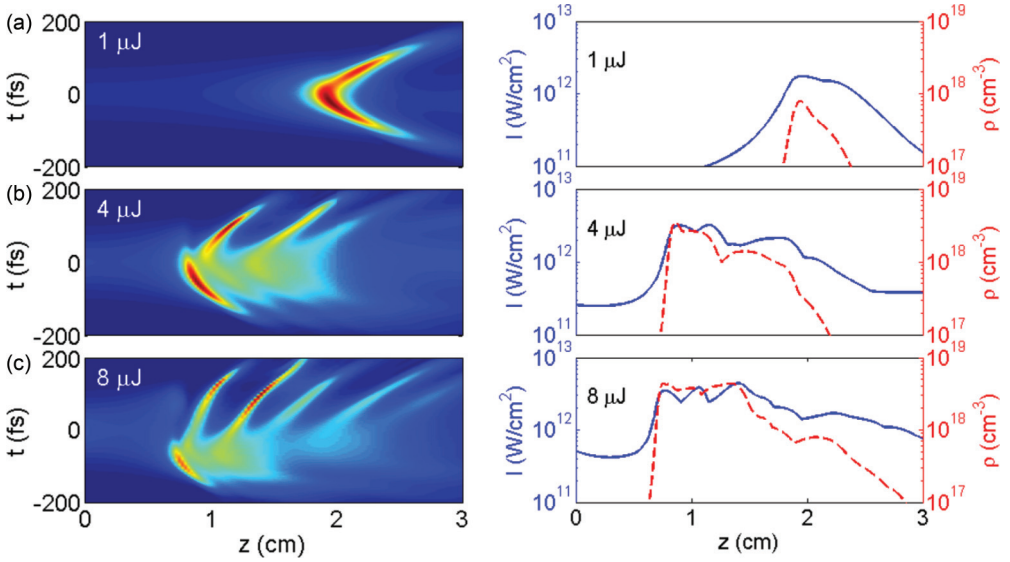

FIG. 10. (Color online) Left: Temporal profiles for the axial intensity distribution $I(t,r = 0,z)$ obtained with $n_2 = 1.7 \times 10^{-16}$ cm^2/W [39] and significantly higher pulse energies with respect to Figs. 8 and 9: (a) 1 μJ, (b) 4 μJ, and (c) 8 μJ. Right: Maximum intensity (solid curves) and electron density (dashed curves) as functions of the propagation distance for the same energies.

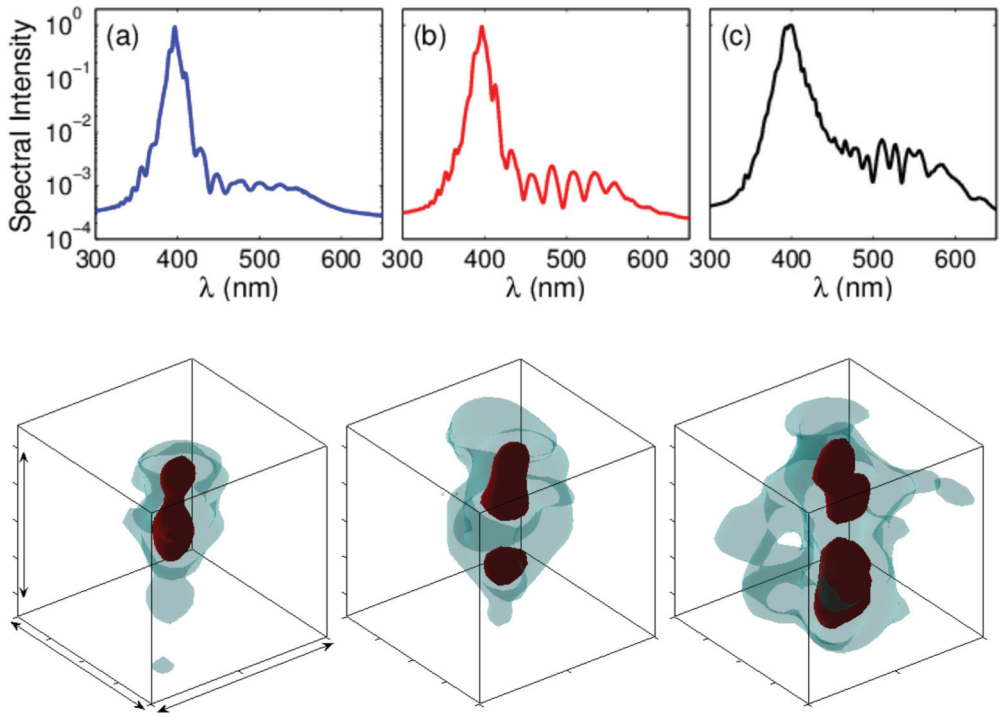

FIG. 11. (Color online) Comparison of supercontinuum spectra (first row) and 3D mapping of the pulse intensity distribution (second row) after propagation in water over 12 mm of a 400-nm pulse focused with L1 = 50 mm. Pulse energy: (a) 300 nJ; (b) 400 nJ; (c) 900 nJ. Lighter (blue) and darker (red) isosurfaces correspond to isointensities equal to 30% and 50% of the maximum intensity, respectively. Propagation direction: from top to bottom. Scales indicated by arrow lengths: 40 μm × 40 μm × 200 fs.

simulated axial intensity profile $I(t,r=0,z)$ for a UV pulse propagating in water as a function of the propagation distance z. In addition to the good agreement for the propagation distances between splitting events, a striking feature of the splitting dynamics is the systematic presence of two split pulses, both in measurements and in simulations. At IR wavelengths, plasma defocusing quickly quenches the trailing pulse and its visibility ceases at longer propagation distances [40]. For UV wavelengths, our results suggest that the main effect responsible for a splitting event is MPA, which acts as a distributed stopper along the propagation axis, both reducing the intense peak in the central part of the beam and generating a ring-like diffraction pattern, as observed in our measurements. The prevailing role of MPA is compatible with the spatial replenishment of the pulse central part [41], since the effect of a stopper is followed by a beam reconstruction similar to that occurring in the Arago spot experiment [42,43]. Transmittance measurements in Fig. 6 also confirm the crucial role of MPA. The plasma generated by the leading split pulse induces defocusing and could also lead to ring formation. However, the systematic observation of coexisting split pulses with nearly the same peak intensity indicates that plasma defocusing does not induce any delay in the formation of the trailing split pulse and therefore plays only a secondary role in the pulse-splitting mechanism. It was also established that the combined effects of plasma defocusing and pulse self-steepening induce a significant spectral broadening toward shorter wavelengths [44]. Our measurements show the opposite, i.e., spectral broadening toward the longer wavelengths in the visible region, interpreted as resulting from a steep pulse leading edge, in keeping with a dominant role of MPA [45]. The main role of MPA is further confirmed by the the fact that spectra were essentially red-shifted after splitting events, whereas plasma defocusing, in conjunction with self-steepening, would be responsible for the generation of new frequencies on the blue side of the laser spectrum.

VI. MEASUREMENTS FOR TIGHTER FOCUSING CONDITIONS

Splitting events were also observed for tighter focusing conditions (L1: 50 mm), although with clearly different and more complex reshaping features (Fig. 11). For the same pulse energy, after a splitting event, bright rings with a nice revolution symmetry are more visible at loose focusing. With the shortest focal length (50 mm), the generic spectral broadening, spectral modulations, and submodulations are retrieved by increasing the pulse energy [see Figs. 11(a)–11(c)]. The temporal and spectral pulse dynamics is therefore not quenched for tighter focusing conditions, leading to similar signatures of laser energy deposition and pulse splitting (see intensity distributions in Fig. 11) as in the case of loose focusing conditions.

VII. CONCLUSION

In conclusion, we have carefully characterized the complete dynamics of ultrashort laser pulses undergoing filamentation in water at 400 nm. We have monitored the transitions in the complex filamentation dynamics involving space-time couplings with recurrent pulse splitting when the focusing geometry is changed from loose to tighter focusing. Filaments

were observed at focusing geometries from NA $\sim 3 \times 10^{-3}$ to NA $\sim 2 \times 10^{-2}$. We recorded intensity maps in space and time at different pulse energies, for a range of propagation distances where relevant nonlinear events occur. We simultaneously recorded transmission, conical emission, and spectral broadening data and we connected the observed space-time transformations of the pulse to specific signatures in transmission curves and spectra. From a solely practical point of view, the supercontinuum spectra and conical emission patterns allow us to easily identify pulse-splitting events without employing a complex experimental apparatus and could be readily used for online monitoring of filamentation dynamics. Pulse splitting was observed in all cases. Low numerical apertures lead to deposition of laser energy in localized nonlinear foci over an elongated focal region, associated with the occurrence of one or several pulse-splitting events depending on the pulse energy. The first event follows a significant nonlinear absorption and is associated with the generation of a smooth, red-shifted supercontinuum and smooth conical emission pattern. Subsequent splitting events consume less energy and induce modulations in supercontinuum spectra and conical emission. Tighter focusing geometries lead to shorter focal regions. Measurements compare favorably with predictions of the dynamic spatial replenishment model [41] and simulation results, indicating a transition in the nature of pulse splitting featuring a prevailing role of MPA when the laser wavelength is changed from the IR to the UV region.

Our results disclose the missing links between a wealth of nonlinear phenomena, which govern the complex space-time dynamics of intense laser pulses propagating in water (and, more generally, in transparent dielectric media) and provide a substantial advance in our understanding of femtosecond laser energy deposition in liquid media. This knowledge is of critical importance for a range of practical applications relying on laser-induced cavitation and its control and constitutes a cornerstone in the general development of nonintrusive methods for femtosecond laser surgery, in particular.

ACKNOWLEDGMENTS

This research was supported by the European Commission Seventh Framework Programme Project LASERLAB-EUROPE II access (Grant Agreement No. 228334). G.T., D.M., and A.D. acknowledge financial support from the European Social Fund under the Global Grant measure (Grant No. VP1-3.1-ŠMM-07-K-03-001).

[1] J. S. D'Souza, J. A. Dharmadhikari, A. K. Dharmadhikari, B. J. Rao, and D. Mathur, Phys. Rev. Lett. **106**, 118101 (2011).
[2] A. Vogel, N. Linz, S. Freidank, and G. Paltauf, Phys. Rev. Lett. **100**, 038102 (2008).
[3] A. Vogel, J. Noack, G. Hüttman, and G. Paltauf, Appl. Phys. B **81**, 1015 (2005).
[4] R. Meesat, H. Belmouaddine, J.-F. Allard, C. Tanguay-Renaud, R. Lemay, T. Brastaviceanu, L. Tremblay, B. Paquette, J. R. Wagner, J.-P. Jay-Gerin, M. Lepage, M. A. Huels, and D. Houde, Proc. Natl. Acad. Sci. U.S.A. **109**, E2508 (2012).
[5] K. Plamann, F. Aptel, C. L. Arnold, A. Courjaud, C. Crotti, F. Deloison, F. Druon, P. Georges, M. Hanna, J.-M. Legeais, F. Morin, E. Mottay, V. Nuzzo, D. A. Peyrot, and M. Savoldelli, J. Opt. **12**, 084002 (2010).
[6] M. Vengris, E. Gabryte, A. Aleknavicius, M. Barkauskas, O. Ruksenas, A. Vaiceliunaite, and R. Danielius, J. Cataract Refr. Surg. **36**, 1579 (2010).
[7] M. Merker, R. Ackermann, R. Kammel, K. S. Kunert, and S. Nolte, Laser. Surg. Med. **45**, 589 (2013).
[8] J. Noack and A. Vogel, IEEE J. Quant. Electron. **35**, 1156 (1999).
[9] Q. Feng, J. V. Moloney, A. C. Newell, and E. M. Wright, Opt. Lett. **20**, 1958 (1995).
[10] C. Schaffer, N. Nishimura, E. Glezer, A. Kim, and E. Mazur, Opt. Express **10**, 196 (2002).
[11] D. Faccio, E. Rubino, A. Lotti, A. Couairon, A. Dubietis, G. Tamošauskas, D. G. Papazoglou, and S. Tzortzakis, Phys. Rev. A **85**, 033829 (2012).
[12] A. C. Bernstein, T. S. Luk, T. R. Nelson, A. McPherson, J.-C. Diels, and S. M. Cameron, Appl. Phys. B **75**, 119 (2002).
[13] A. C. Bernstein, J.-C. Diels, T. S. Luk, T. R. Nelson, A. McPherson, and S. M. Cameron, Opt. Lett. **28**, 2354 (2003).
[14] M. Wittmann and A. Penzkofer, Opt. Commun. **126**, 308 (1996).
[15] A. Brodeur and S. L. Chin, Phys. Rev. Lett. **80**, 4406 (1998).
[16] A. Couairon and A. Mysyrowicz, Phys. Rep. **441**, 47 (2007).
[17] A. Dubietis, G. Tamošauskas, I. Diomin, and A. Varanavičius, Opt. Lett. **28**, 1269 (2003).
[18] W. Liu, O. Kosareva, I. S. Golubtsov, A. Iwasaki, A. Becker, V. P. Kandidov, and S. L. Chin, Appl. Phys. B **76**, 215 (2003).
[19] D. Faccio, A. Matijosius, A. Dubietis, R. Piskarskas, A. Varanavičius, E. Gaižauskas, A. Piskarskas, A. Couairon, and P. Di Trapani, Phys. Rev. E **72**, 037601 (2005).
[20] M. A. Porras, A. Dubietis, E. Kučinskas, F. Bragheri, V. Degiorgio, A. Couairon, D. Faccio, and P. Di Trapani, Opt. Lett. **30**, 3398 (2005).
[21] S. Minardi, A. Gopal, M. Tatarakis, A. Couairon, G. Tamosauskas, R. Piskarskas, A. Dubietis, and P. D. Trapani, Opt. Lett. **33**, 86 (2008).
[22] S. Minardi, A. Gopal, A. Couairon, G. Tamosauskas, R. Piskarskas, A. Dubietis, and P. D. Trapani, Opt. Lett. **34**, 3020 (2009).
[23] M. Kolesik, G. Katona, J. V. Moloney, and E. M. Wright, Phys. Rev. Lett. **91**, 043905 (2003).
[24] M. Kolesik, E. M. Wright, and J. V. Moloney, Phys. Rev. Lett. **92**, 253901 (2004).
[25] D. Faccio, M. Porras, A. Dubietis, F. Bragheri, A. Couairon, and P. Di Trapani, Phys. Rev. Lett. **96**, 193901 (2006).
[26] S. Tzortzakis, D. G. Papazoglou, and I. Zergioti, Opt. Lett. **31**, 796 (2006).
[27] D. Faccio, M. Clerici, A. Averchi, O. Jedrkiewicz, S. Tzortzakis, D. G. Papazoglou, F. Bragheri, L. Tartara, A. Trita, S. Henin, I. Cristiani, A. Couairon, and P. Di Trapani, Opt. Express **16**, 8213 (2008).
[28] A. Matijošius, J. Trull, P. Di Trapani, A. Dubietis, R. Piskarskas, A. Varanavičius, and A. Piskarskas, Opt. Lett. **29**, 1123 (2004).
[29] D. Majus, V. Jukna, G. Tamosauskas, G. Valiulis, and A. Dubietis, Phys. Rev. A **81**, 043811 (2010).

[30] M. A. C. Potenza, S. Minardi, J. Trull, G. Blasi, D. Salerno, A. Varanavicius, A. Piskarskas, and P. Di Trapani, Opt. Commun. **229**, 381 (2004).
[31] B. Prade, M. Franco, A. Mysyrowicz, A. Couairon, H. Buersing, B. Eberle, M. Krenz, D. Seiffer, and O. Vasseur, Opt. Lett. **31**, 2601 (2006).
[32] S. L. Chin, F. Théberge, and W. Liu, Appl. Phys. B **86**, 477 (2007).
[33] A. Couairon, E. Brambilla, T. Corti, D. Majus, O. de J. Ramírez-Góngora, and M. Kolesik, Eur. Phys. J. Special Topics **199**, 5 (2011).
[34] K. D. Mielenz, Appl. Opt. **17**, 2875 (1978).
[35] R. W. Boyd, *Nonlinear Optics* (Academic Press, New York, 2008).
[36] L. V. Keldysh, Zh. Eksp. Teor. Fiz. **47**, 1945 (1964) [Sov. Phys. JETP **20**, 1307 (1965)].
[37] P. K. Kennedy, IEEE J. Quant. Electron. **31**, 2241 (1995).
[38] D. N. Nikogosyan, *Properties of Optical and Laser-Related Materials* (Wiley, Chichester, UK, 1997).
[39] Z. W. Wilkes, S. Varma, Y.-H. Chen, H. M. Milchberg, T. G. Jones, and A. Ting, Appl. Phys. Lett. **94**, 211102 (2009).
[40] A. Couairon, E. Gaižauskas, D. Faccio, A. Dubietis, and P. Di Trapani, Phys. Rev. E **73**, 016608 (2006).
[41] M. Mlejnek, E. M. Wright, and J. V. Moloney, Opt. Lett. **23**, 382 (1998).
[42] A. Dubietis, E. Gaižauskas, G. Tamošauskas, and P. Di Trapani, Phys. Rev. Lett. **92**, 253903 (2004).
[43] A. Dubietis, E. Kučinskas, G. Tamošauskas, E. Gaižauskas, M. A. Porras, and P. Di Trapani, Opt. Lett. **29**, 2893 (2004).
[44] A. L. Gaeta, Phys. Rev. Lett. **84**, 3582 (2000).
[45] F. Bragheri, D. Faccio, A. Couairon, A. Matijosius, G. Tamošauskas, A. Varanavičius, V. Degiorgio, A. Piskarskas, and P. Di Trapani, Phys. Rev. A **76**, 025801 (2007).